ELSEVIER

Experimental Thermal and Fluid Science 24 (2001) 61–66

Experimental Thermal and Fluid Science

www.elsevier.nl/locate/etfs

Low Reynolds-number moment on asymmetric bodies

Kurt O. Lund *, Dietmar Trees [1]

Department of Mechanical and Aerospace Engineering, Center for Energy Research, University of California, La Jolla, CA 92093-0417, USA

Received 9 June 1999; accepted 12 May 2000

Abstract

The moment induced on asymmetric particles by a low Reynolds-number flow is examined. A flat disk and a half sphere are suspended in low-velocity airflow and the moment exerted on the particles is measured as a function of Reynolds number and approach angle. Object Reynolds-numbers range between 20 and 200, and the measured moment is in the nNm range. A moment coefficient (a moment normalized with the drag force and object radius) is calculated from the moment measurements and found to generally decrease with increasing Reynolds number. Stable approach angle positions are identified for the objects in the flow, and it is shown that the objects tend to rotate towards the position of maximum drag (local extremum) from other approach angles. The present measurements are consistent with previous qualitative observations of free-falling particles.

Keywords: External flow; Asymmetric bodies; Low Reynolds number; Fluid moment; Torque; Moment coefficient; Fluid drag; Torsion balance; Suspended particles; Oscillation; Nano-scale torque

1. Introduction

The angular stability, or rotation, of solid particles immersed in a flow is important for many processes [1,6]. Modern processes involving particle spheres include the growth and dissolution of silicon on spheres, as discussed by Schmidt [7], and a novel application of microcircuits on such spheres (spherical chips) was recently presented [2].

In particular, Becker [1] and Marchildon et al. [6] visually studied the motion and rotation of non-symmetric particles by dropping them in a column of liquid and observing their trajectories. However, these studies emphasized the drag on the particles, and only *qualitative* information was gathered for the rotation, or secondary motion. Becker [1] found that the motion depended on the particle Reynolds number, as follows: in the range $5.5 < Re < 200$, the particles would tend to rotate toward their angular orientations of maximum drag, whereas in the range $200 < Re < 500$, the particles would tend to wobble with uncertain angular orientations. Marchildon et al. [6] identified a lower transition range, $0.05 < Re < 100$, where their cylindrical particles would likewise rotate to a preferred orientation, and an upper transition range, $100 < Re < 1000$, where a secondary motion would set in.

Other studies have emphasized particle drag [5], behavior in fully turbulent flow [3], and slip velocity [4], but there appear no quantitative studies for rotation of particles in the lower transition regime. The general objective of the present work is to provide *quantitative* data for flow-induced moments about asymmetric particles.

The flow of a fluid about a non-symmetric body gives rise to an aerodynamic drag, as well as to differential pressures which induce a net moment or torque on the body. This moment may result from asymmetric pressure fields alone (at very low Reynolds numbers), or in combination with asymmetric and periodic flow-separation, resulting, for example, from the von Karman vortex street. In the latter case, there would tend to be fluid–particle coupling for freely suspended particles.

In the present work, in order to obtain quantitative particle moment data, the "particle" is suspended in the flow field by two torsion wires, and the size of the particle is selected as about 5 cm. A round, flat disk and a half-sphere were selected for the tests conducted in air. Because of this size, and interest in the lower transition

* Corresponding author.

E-mail address: klund@electriciti.com (K.O. Lund).

[1] Present address: Hamilton Sundstrand, A United Technologies Company, 4400 Ruffin Road, P.O. Box 85757, San Diego, CA 92186-5757.

0894-1777/01/$ - see front matter
PII: S0894-1777(00)00058-3

Nomenclature

A_p	projected frontal area (m^2)
C_D	drag coefficient (−)
$C_{D,m}$	constant drag-coefficient magnitude (−)
C_M	moment coefficient (−)
$C_{M,m}$	constant moment-coefficient magnitude (−)
D	object diameter (m)
D_w	wire diameter (m)
f	moment variation function (−)
F_D	drag force (N)
F_B	buoyancy force (N)
g	gravitational acceleration (m/s^2)
G	wire torsional modulus (Pa)
I	particle moment of inertia (kg m^2
J	wire second moment of area (m^4)
L	length (m)
m	particle mass (kg)
M	flow-induced moment (Nm)
M_m	constant moment magnitude (Nm)
p	drag variation function (−)
R_0	object radius (m)
Re	Reynolds number (−)
R_p	center of pressure radius (m)
t	time (s)
t_c	time constant (s)
V	duct average velocity (m/s)
X	detector displacement (m)
Y	distance of falling particle (m)
y	Y/R_0 (−)

Greeks

ϕ	object twist angle
θ	angle of approach
ν	kinematic viscosity
ρ	fluid density (kg/m^3)
ρ_s	solid density (kg/m^3)
τ	scaled time, t/t_c

regime, the approach velocities were very small (∼0.05 m/s), as were the induced moments (∼10 nNm), which necessitated extreme care in collecting the data from a very sensitive torsional balance apparatus.

2. Experimental apparatus

The experiments were conducted in an acrylic flow duct with a diameter of 15 cm, as shown in Fig. 1. The flow entering the duct from the left in Fig. 1 is baffled and passes through a flow straightener before encountering the test object located 30 cm downstream of the straightener. The inlet flow was computer-controlled with a mass flowmeter (0–100 l/min range), to yield object Reynolds numbers on the order of 20–200. This arrangement provided for an average approach velocity closely related to the measured volumetric flow, even though the test objects are a significant fraction of the duct area; the available instrumentation and apparatus did not permit velocity traverses for these low velocities.

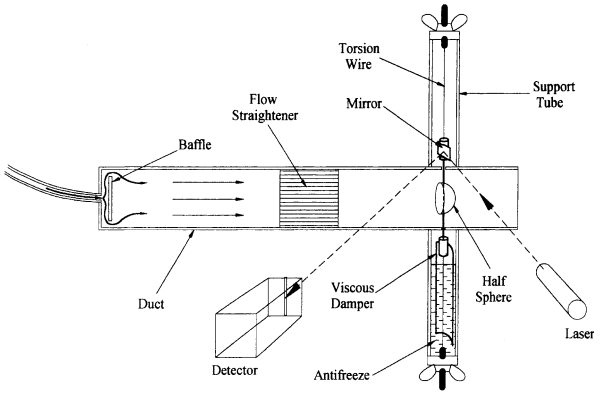

Fig. 1. Experimental apparatus.

The test object with reflection mirror was suspended by two lengths of 0.2 mm torsion wire under tension, thus creating a torsion balance, as shown in Fig. 1. The torsion wires were mounted inside acrylic support tubes attached to the flow duct, in order to avoid possible disturbances. The lower support tube was filled with viscous liquid (antifreeze), and the mounting rod fitted with a damper, to create viscous damping of the object angular displacement, thus stabilizing the detector reading; for the aluminum flat disk, this resulted in a logarithmic decrement of 0.235, or a damping ratio of 0.037.

A fixed laser beam was directed onto the mirror, which resulted in a reflected signal to the detector depending on the angular position of the mirror, mounting rod, and test object. A photo-electric detector was mounted on an optical bench about 2.5 m away from the flow duct, and was provided with micrometer adjustment normal to the reflected laser beam. A thin razor-slit in the detector aperture was made to facilitate precise location of the detector-head on the bench; this location was measured with a dial indicator with a precision of ±0.01 mm. With this experimental setup, displacement angles as small as 10 μrad (2 s of arc) could be determined. By the torsional compliance of the wires, the moment resulting from each rotation-displacement was calculated. The moments induced on the test objects were very small (on the order of 10^{-9} Nm), which necessitated use of this extremely sensitive detection device.

3. Experimental approach

Two objects were tested: a flat circular disk (55.5 mm dia. × 9.7 mm thick), and a half-sphere (55.0 mm dia.). Each object, in turn, was carefully fixed onto the mounting rod with the mirror, and thus suspended between the torsion wires at various angles θ relative to the

oncoming flow (see Fig. 4(a)). For each angular orientation, the flow was stepped up through about eight values, and stepped back down to zero, with the detector position recorded for each flow value. Because of the damping, the reflected beam came to rest in 3–4 oscillations; however, the angular deflection was repeatable only to ±0.05 mm of detector location. On the whole, the setup was very sensitive to surrounding disturbances, and great care and numerous repetitions were required to obtain reliable nNm moment data.

The angle of twist is measured by the displacement, X, of the laser beam on the detector, $\phi = X/2L_b$, where L_b is the length of the beam (~2.5 m). ϕ is further related to the applied moment, M, by the properties of the wires: $\phi = ML_w/GJ$, where L_w is the combined length of the two wires, $1/L_w = 1/L_1 + 1/L_2$, G is the torsional modulus, and J is the wire second moment of area, $J = \pi D_w^4/32$. Thus, the moment induced by the flow is $M = GJX/2L_wL_b$. This moment varies with the Reynolds number, $Re = VD/\nu$, where V is the approach velocity, D is the test-object diameter, and ν the viscosity of air. Both the disk and the half-sphere were suspended through their respective centroids. In this arrangement, the uncertainty of X is about ±5%; since the other parameters were the same for all test measurements, this leads to a ±5% uncertainty in the moment for data points relative to one another. On an absolute scale, considering variations in properties and other dimensions, the uncertainty is estimated as ±10%.

The flow-induced moment can be thought of as being made up of the net drag force F_D acting through a center of pressure displaced by R_p from the centroidal axis: $M = F_DR_p = 1/2\rho V^2C_D(\pi R_0^2)R_p$. If the moment coefficient is taken as $C_M = C_DR_p/R_0$, then it is defined through the following equation:

$$M \equiv \frac{\pi}{2}\rho V^2R_0^3C_M = \frac{\pi}{16}\rho V^2D^3C_M. \quad (1)$$

With M (or C_M) determined from the present experiments (and with known or estimated drag coefficients), this provides an estimate of the center of pressure location.

4. Results and discussion

4.1. Flat disk

The initial data for the flat disk inclined at $\theta = 38.7°$ to the oncoming flow is shown in Fig. 2, up to $Re > 400$. There is a regular increase in M with Re, as seen, but for $Re > 250$ there were progressively stronger oscillations of the disk, which necessitated the averaging of readings.

This oscillation is indicative of the periodic vortex shedding of the Karman vortex street (where vortices separate from alternate sides of the disk), and may also involve fluid-elastic coupling with the torsion system. For the flat Aluminum disk, the natural frequency of the torsion system was found to be ~0.4 Hz, which corresponds to the Strouhal vortex-shedding frequency at $Re \sim 375$. Thus, at the higher Reynolds numbers there would be lock-in of the vortex shedding and the test-object motion. This oscillatory behavior is consistent with earlier visual observations [1,6]. The remainder of the test data is for small Re where any vortex shedding is below the system natural frequency.

The data obtained for the flat disk are summarized in Fig. 3(a) as $C_M(Re)$. This plot has the same character-

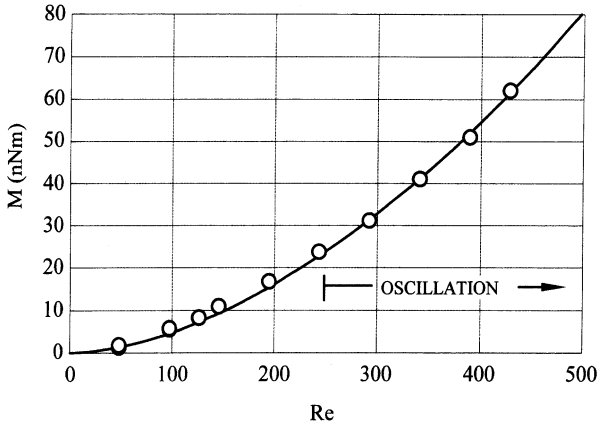

Fig. 2. Flat-disk moments for $\theta = 38.7°$.

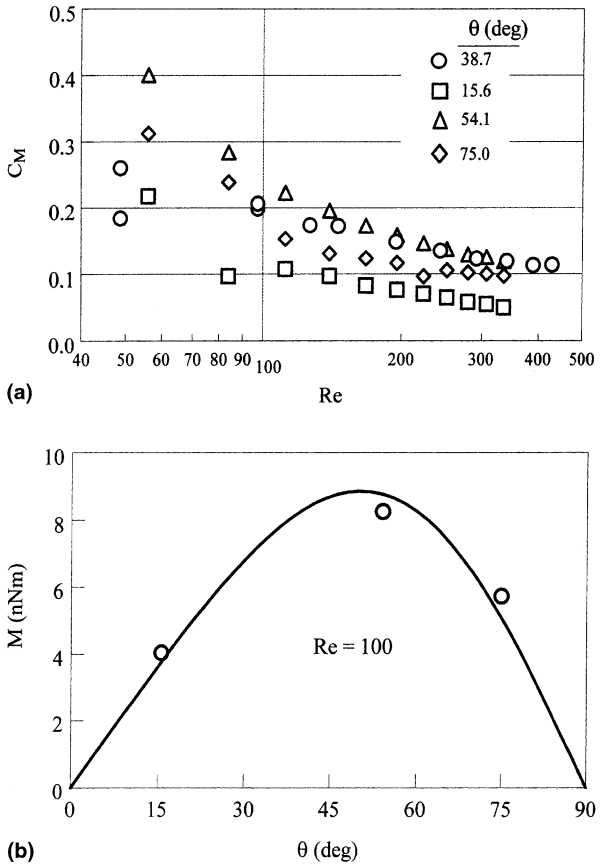

Fig. 3. (a) Flat-disk moment coefficients vs. Reynolds number. (b) Flat-disk moment coefficient vs. approach angle.

istic as drag coefficients, with the coefficient decreasing with increasing *Re* for small Reynolds numbers (and suggests a constant R_p location). Increased scatter of the data is seen as *Re* falls below 100. The maximum moment is for $\theta \approx 50°$, with lesser values for approach angles smaller or greater than this value, as shown in Fig. 3(b). The disk has axes of symmetry at $\theta = 0$ and 90°; therefore, M and C_M tend to zero for these two angles. It is seen that for $0 < \theta < 90°$, the moments and coefficients are always in the direction of the angular displacement (always positive), thus tending to rotate the disk toward its position of maximum drag, as noted previously.

Fig. 3(b) shows the moment as a function of θ for $Re = 100$, compared to a smooth, periodic curve. A perturbation from the position of maximum drag ($\theta = 90°$) towards a greater approach angle will create a negative moment, thus forcing the disk back to its maximum drag position; a similar restoring moment is produced for perturbations below 90°. Thus, the maximum drag angular position is one of stable equilibrium. By contrast, the position of minimum drag ($\theta = 0°$) is unstable equilibrium.

4.2. Half-sphere

In the case of the half-sphere, there is only symmetry at $\theta = \pm 90°$. Hence, the results will differ according to whether the flow approaches from the spherical side (positive θ), or the flat side (negative θ).

In Fig. 4(a) are shown the moments for several *positive* angles, which are in the same direction as the angular position, θ. At the highest *Re* the maximum moment occurs for the smallest angle θ, but at the lowest *Re* this is reversed; thus, the *Re* and θ dependencies are coupled.

In Fig. 4(b) are shown the moments for several *negative* angles, which are also in the same direction as the angular position, θ. Again, there is a reversal of the θ dependence at different Reynolds numbers.

The positive and negative aspects of the induced moments are summarized in Fig. 5 as C_M *(Re)*. At the lowest Reynolds numbers the moment coefficients are quite uncertain, but the sense of the moments is consistent and accurate. Thus, for the half-sphere with two distinct drag maxima, the induced moment is in the direction toward maximum drag too, whether "positive" or "negative".

The periodic nature of the induced moment is shown in Fig. 6 in variation with the approach angle, θ, for $Re = 100$, and in comparison to a fitted periodic curve. It is clear that the moment for an object must be periodic in θ with period 2π ; for a half-sphere, symmetry additionally requires the moment to be zero at $\theta = \pm 90°(\pm\pi/2)$. A function which satisfies these conditions and $M(\theta + \pi/2) = -M(\theta)$ is given by the sine series:

$$M = M_m f(\theta); \quad f(\theta) \equiv \sum_{i=1}^{n} a_i \sin(i\{\theta + \pi/2\}), \tag{2}$$

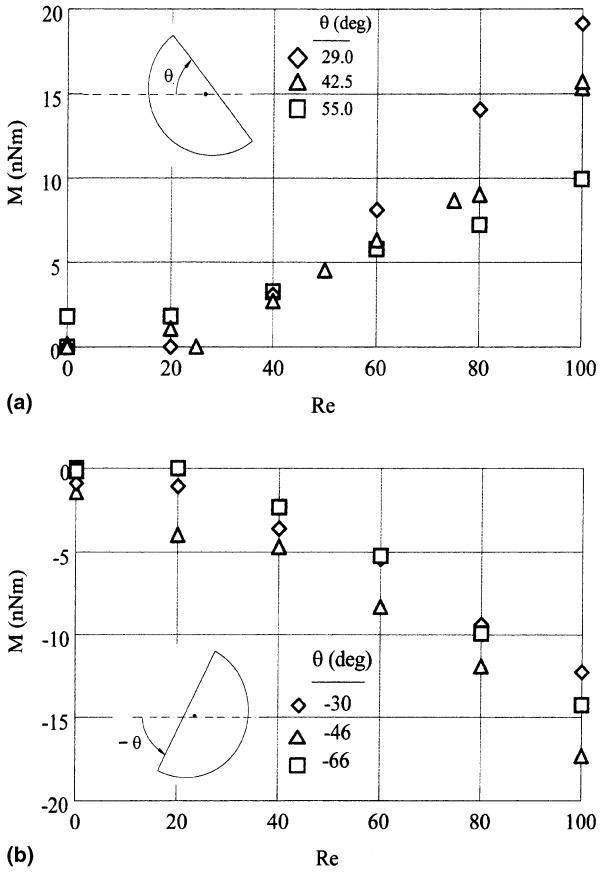

Fig. 4. (a) Half-sphere positive moments vs. Reynolds number. (b) Half-sphere negative moments vs. Reynolds number.

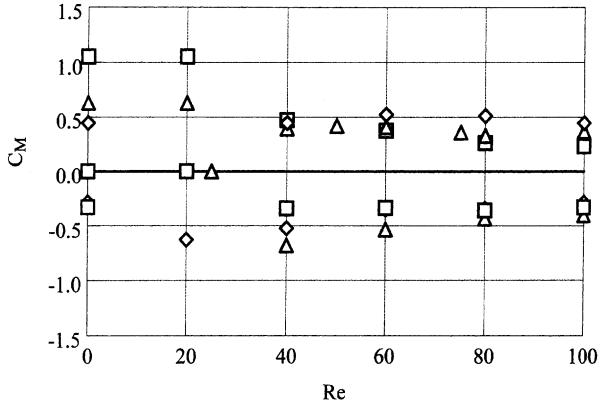

Fig. 5. Half-sphere moment coefficients (symbols as per Fig. 4).

where M_m is a constant moment magnitude. The curve in Fig. 6 is based on $M_m = 20$ nNm and the first five coefficients of (2),

i	1	2	3	4	5
a_i	0.282	−0.804	−0.366	0.092	0.055

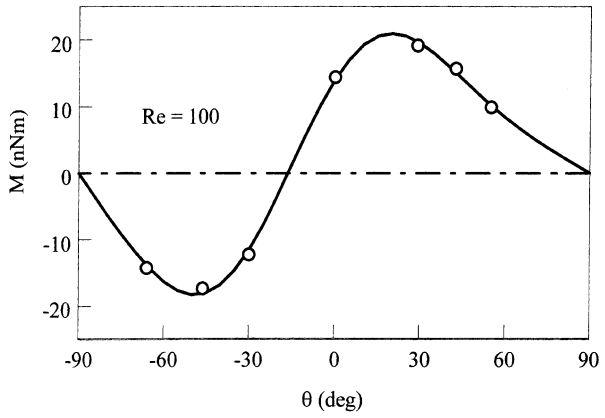

Fig. 6. Half-sphere moments vs. approach angle.

which emphasizes a consistent, periodic variation of M with θ, and the directional aspect of M. Measurements were also performed for $\theta = 0$, which resulted in non-zero moments because of non-symmetry, as shown in Fig. 6 (by comparison, the moment for the flat disk at this angle is zero because of its symmetry). In Fig. 6, the stable conditions for the half sphere are at its maximum drag positions, $\pm 90°$; the zero at $-16.4°$ is unstable, as seen by comparison of the slopes with those in Fig. 3(b). Like the case of the flat disk, perturbations from these angles cause moments in the opposite direction, thus turning the half-sphere back to its maximum drag position.

5. Application

The rate of rotation of asymmetric particles is important for a variety of processes; for example, where the particle is injected into a stream, or falling through a fluid [1,6]. For illustration we consider the latter case where a half-sphere falls through a fluid; then, with $F = m\ddot{Y}$ and $M = I\ddot{\theta}$, the equations of motion are

$$mg - F_B - F_D \equiv m'g - \frac{\pi}{2}\rho V^2 R_0^2 C_D = m\ddot{Y}, \tag{3a}$$

$$M \equiv \frac{\pi}{2}\rho V^2 R_0^3 C_M = I\ddot{\theta}, \tag{3b}$$

or, with application to a half-sphere where $m = 2\pi\rho_s R_0^3/3$ and $I = 2mR_0^2/5$

$$\ddot{y} = \frac{g}{R_0}(1 - \rho/\rho_s) - \frac{3}{4}(\rho/\rho_s)\dot{y}^2 C_D(\dot{y}, \theta) \tag{4a}$$

$$\ddot{\theta} = (15/8)(\rho/\rho_s)\dot{y}^2 C_M(\dot{y}, \theta). \tag{4b}$$

Thus, there is coupling between the linear and angular motions of the particle. For the present illustration, we consider the axial acceleration in Eq. (4a) to be negligible (terminal velocity condition of particle); then from Eq. (4b), the rate of rotation is given by

$$\begin{aligned}\frac{d^2\theta}{dt^2} &= \frac{5}{2}\frac{g}{R_0}\left(1 - \frac{\rho}{\rho_s}\right)\frac{C_M(\theta)}{C_D(\theta)} \\ &\approx \frac{5}{2}\frac{g}{R_0}\left(1 - \frac{\rho}{\rho_s}\right)\frac{C_{M,m} f(\theta)}{C_{D,m} p(\theta)}.\end{aligned} \tag{5a}$$

Here the form of the moment coefficient, $f(\theta)$, was taken from Eq. (2), and the drag coefficient was assumed to vary as the projected frontal area, which for the first quadrant is

$$A_p/\pi R_0^2 \equiv p(\theta) = \sin\theta + [\pi - 2\theta - \sin(\pi - 2\theta)]/2\pi.$$

Let $\tau = t/t_c$ where the time constant is

$$t_c^{-2} = \frac{5}{2}\frac{g}{R_0}\left(1 - \frac{\rho}{\rho_s}\right)\frac{C_{M,m}}{C_{D,m}}$$

then, Eq. (5a) becomes

$$\frac{d^2\theta}{d\tau^2} = \frac{f(\theta)}{p(\theta)}. \tag{5b}$$

The numerical solution of Eq. (5b) is shown in Fig. 7(a) for various initial conditions, θ_0. Starting at $\theta_0 = 45°$ (upper solid curve), there is a positive forcing moment which causes the increase in θ; from Fig. 6, this moment becomes negative beyond 90°, thus slowing down the increase in θ. However, the inertia of the particle causes θ to overshoot 90° and increase to a maximum of 135°;

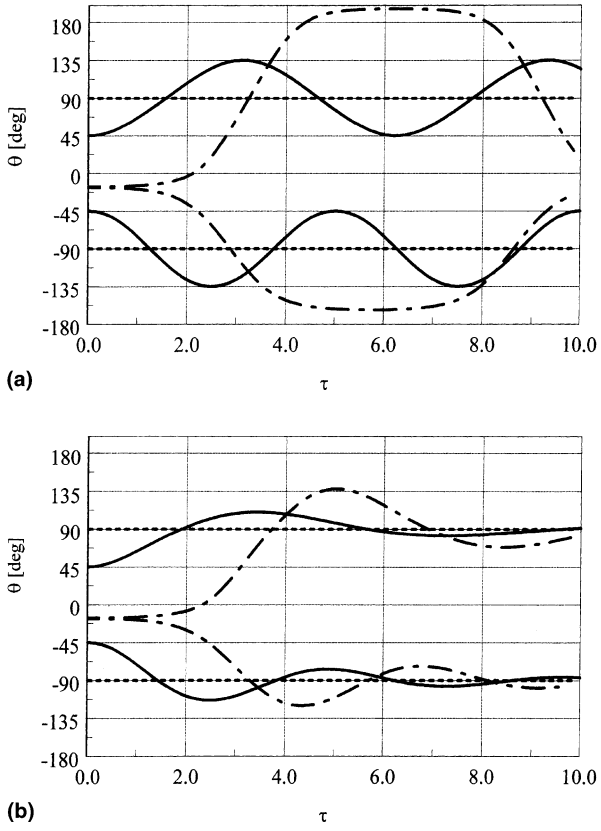

Fig. 7. (a) Angular positions for falling particles (without damping). (b) Angular positions for falling particles (with damping).

this results in particle oscillation about the maximum drag angle of 90°, as seen. A similar behavior occurs for $\theta_0 = -45°$ (lower solid curve).

When $\theta_0 = \pm 90°$, the forcing function in Eq. (5b) is zero, and there are no angular changes calculated for these stable orientations (dashed lines). Slight variations in θ_0 (e.g., $\theta_0 = \pm 85°$) likewise resulted in only slight variations of θ from the stable orientations, $\pm 90°$.

The two other initial conditions, shown in Fig. 7(a) as the dot–dash curves, are for $\theta_0 = -16°$ and $-17°$ near the present neutral angle of $-16.4°$. Here, the small variations from the neutral position produces corresponding small driving moments, thus delaying rotation. However, even small variations from this unstable neutral position eventually cause larger rotation and oscillation, as seen.

It appears from Fig. 7(a) that particle oscillations would continue undiminished and indefinitely. This is predicted because of the lack of rotational damping in the model, Eq. (5b). If a linear damping term is added to Eq. (5b), with a damping ratio of 0.5, then the curves appear as in Fig. 7(b). Now, it is seen that rotations tend toward the two maximum drag locations, as expected. Thus, the experimentally observed low-*Re* rotations to maximum drag angles [1,6] are predicted by the present measurements and correlations.

6. Conclusion

A delicate experiment has been performed for the quantitative determination of the moment experienced by asymmetrical particles in low-*Re* flow. The test results show that steady, flow-induced moments increase uniformly with Reynolds numbers in the low-*Re* regime ($Re < 200$), and vary periodically with angle of approach (with the sense of the moment the same as the angular displacement); moment coefficients were found to be on the order of 0.5, and relatively insensitive to *Re* variations. In the high-*Re* regime, unsteady and oscillatory moments resulted (due to vortex shedding).

A simple, dynamical model was constructed from the measurements to illustrate the likely behavior of a half-sphere under terminal, free-fall conditions. Although approximate, the model shows the rotation of the particle tending to the local maximum-drag position. The present quantitative measurements and calculations are consistent with previous qualitative observations.

Acknowledgements

The authors wish to acknowledge the generous support provided by SML Associates, Encinitas, California (Mr. S.M. Lord, President), as well as the students who constructed the apparatus: Messrs. Quoc Lee, Tung Huang, Huy Nguyen, and Carlos Cruz; also, the assistance of Mr. Huy Nguyen in providing several figures for this paper is much appreciated.

References

[1] H.A. Becker, The effects of shape and Reynolds number on drag in the motion of a freely oriented body in an infinite fluid, Can. J. Chem. Eng. (1959) 85–91.
[2] Economist News Magazine, 25 St. James Street, London, SW1A 1HG, December 5–11 (1998) 100.
[3] S.K. Friedlander, Behavior of suspended particles in a turbulent fluid, A.I.Ch.E.J. 3 (3) (1957) 381–385.
[4] J.H. Jones et al., Slip velocity of particulate solids in vertical tubes, A.I.Ch.E.J. 12 (6) (1966) 10770–11074.
[5] Y.D. Ju, R.L. Shambaugh, Air drag on fine filaments at oblique and normal angles to the air stream, Polymer Eng. Sci. 34 (12) (1994) 958–964.
[6] E.K. Marchildon, A. Clamen, W.H. Gauvin, Drag and oscillatory motion of freely falling cylindrical particles, Can. J. Chem. Eng. (1964) 178–182.
[7] L.D. Schmidt, The Engineering of Chemical Reactions, Oxford University Press, Oxford, 1998, pp. 382.